Journal of Geodynamics 90 (2015) 42–57

Contents lists available at ScienceDirect

Journal of Geodynamics

journal homepage: http://www.elsevier.com/locate/jog

Seismotectonic analysis of the 2013 seismic sequence at the western Corinth Rift

G. Chouliaras [a], I. Kassaras [b,*], V. Kapetanidis [b], P. Petrou [a], G. Drakatos [a]

[a] Institute of Geodynamics, National Observatory of Athens, Lofos Nymfon, 11810 Athens, Greece
[b] Department of Geophysics-Geothermics, University of Athens, 15784 Athens, Greece

ARTICLE INFO

Article history:
Received 17 October 2014
Received in revised form 9 July 2015
Accepted 13 July 2015
Available online 30 July 2015

Keywords:
Seismic swarm
Spatiotemporal
Seismotectonics
Normal faulting
Corinth Rift

ABSTRACT

This study focuses on a series of small intraplate earthquakes that took place during May–August 2013 on the southwestern coast of the Corinth Rift (Central Greece), a few km southeast of Aigion city. The Corinth Rift is one of the most seismically active parts of the Mediterranean. We analyzed more than 1500 events with $0.4 \leq M_L \leq 3.7$, the major part of which was recorded by a dense local network. The seismicity is densely clustered in a volume of dimensions $\sim 4 \times 2 \times 6\,km^3$, aligned in a N110° direction and at depths ranging between 6 and 12 km. Precisely relocated hypocenters and reliably constrained focal mechanisms indicate north dipping planar faults with an average dip of ~60°. Stress inversion of focal mechanisms implies that the dominant local stress field is extensional in a N5° direction, in good agreement with geodetic observations. The swarm evolved in two phases, with a spatiotemporal migration of epicenters from the eastern toward the western part of the rupture zone, while slip distribution appears homogeneous over the eastern part and strongly inhomogeneous in the western part. These two phases also produced different results in scaling relations such as the Gutenberg–Richter law, the Modified Omori Formula and the Epidemic Type of Aftershock Sequence model. Similar results from other studies have been reported and correlated with a fluid driven mechanism, however further research is required to strengthen this hypothesis for the purposes of this study.

1. Introduction

The present study concerns the seismotectonic analysis of a large sequence of small earthquakes that took place on the western Corinth Rift in Central Greece, over a three month period in 2013. The Corinth Rift is a prevailing extensional tectonic structure with a length of 110 km in a N120° direction and is classified as one of the most seismically active areas in Europe (Fig. 1).

Crustal extension in the Corinth Rift has been attributed to a combination of three major scale processes involving: the back arc extension due to the Hellenic Trench subduction zone (Doutsos et al., 1988), the propagation of the North Anatolian fault within the Aegean (Armijo et al., 1996) and the gravitational collapse of the overloaded crust after the Hellenides orogeny phase (Jolivet, 2001).

The Corinth Rift is a young tectonic rift (1–2 My) (Bell et al., 2009) comprised of E–W striking normal faults that are located onshore to the north and south and offshore in-between. The faulting is mainly composed of 10–20 km long *en echelon* segments, with dip angles 50–70° with a southward dip on the northern shore and a northward dip on the southern shore (Fig. 2) (Micarelli et al., 2003; Moretti et al., 2003; McNeill et al., 2005a; Bell et al., 2008).

The deformation demonstrated by GPS surveys shows a very high horizontal strain rate in a N–S direction, equal to about $10\,mm\,y^{-1}$ in the eastern part of the Rift, $14\,mm\,y^{-1}$ in the central part and $15\,mm\,y^{-1}$ in the western part (Clarke et al., 1998; Briole et al., 2000; Avallone et al., 2004). In addition, an uplift rate of more than $1\,mm\,y^{-1}$ has been reported on the southern shore and Holocene subsidence ($1.3–2.5\,mm\,y^{-1}$) offshore (De Martini et al., 2004; McNeill et al., 2005b, 2007; Palyvos et al., 2008). The E–W increase in strain rates has not been constant during the Corinth Rift's history and the step-like increase in the amplitude of the extension rate is related to shifts in the loci of maximum extension (Bell et al., 2011), to reach the present day kinematic rates (Ford et al., 2013). The rapid growth and offshore fault development in the western part of the rift, has been suggested to be the result of strain transfer between segments of the major sub-parallel faults of western Heliki and Aigion (McNeill et al., 2007).

The syn-rift deformation within the western Corinth Rift has been investigated by many researchers (McNeill et al., 2005a, 2007;

* Corresponding author.
E-mail address: kassaras@geol.uoa.gr (I. Kassaras).

http://dx.doi.org/10.1016/j.jog.2015.07.001
0264-3707/

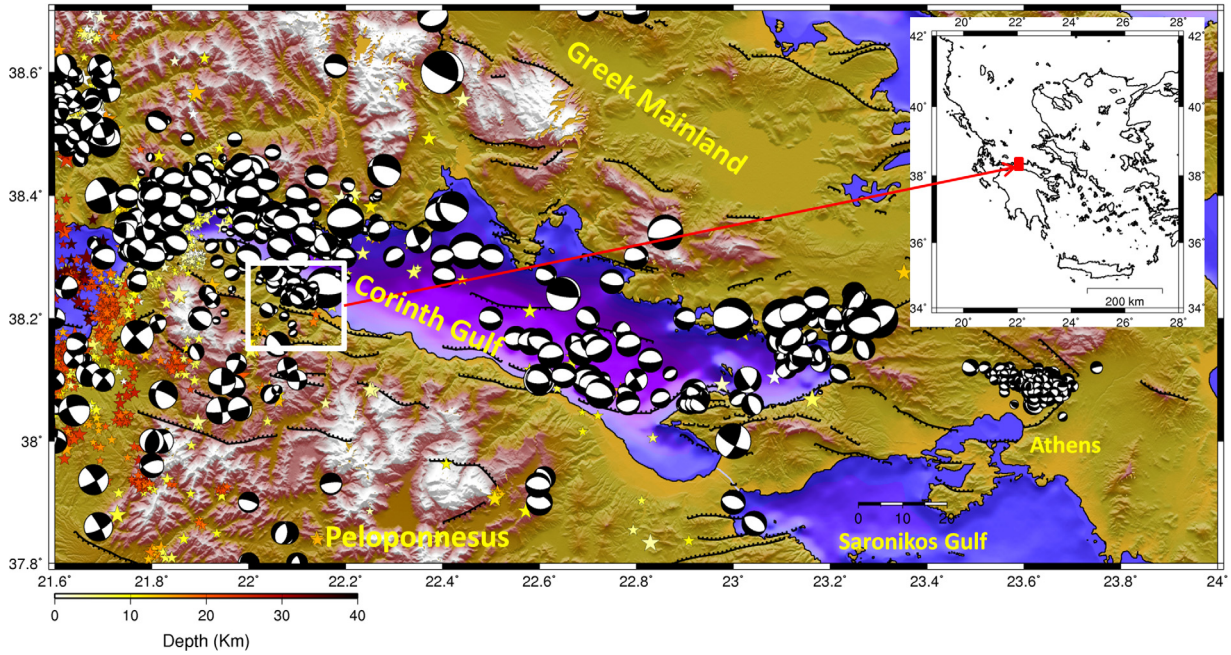

Fig. 1. Map showing the main tectonic features of the Corinth Rift that includes epicenters of instrumentally recorded earthquakes with Ms ≥ 4.0 (1900–2013, Makropoulos et al., 2012, NOAGI – http://bbnet.gein.noa.gr) and available focal mechanisms (1861–2013) from Papazachos and Papazachou (2003) NOAGI (http://bbnet.gein.noa.gr/HL/database), Harvard (http://www.globalcmt.org), Vannucci and Gasperini (2004), Papadimitriou et al. (1994, 2002), Hatzfeld et al. (2000). Barbed lines are active faults (Armijo et al., 1996). The white rectangle shows the position of the study area. The embedded map in the upper right corner of the panel shows the position of the study area within the Greek territory.

Bell et al., 2008, 2009; Taylor et al., 2011; Beckers et al., 2015). An interesting discussion concerns the role of low-angle faults and detachments in the western Corinth Rift and their association with the steeply dipping faults that are observed on and off shore. A low-angle detachment zone with a dip 15–20° has been suggested to be located offshore at depths between 6 and 9 km, in order to accommodate the measured strain rates (Rigo et al., 1996; Bernard et al., 1997; Briole et al., 2000). On the other hand, the absence of

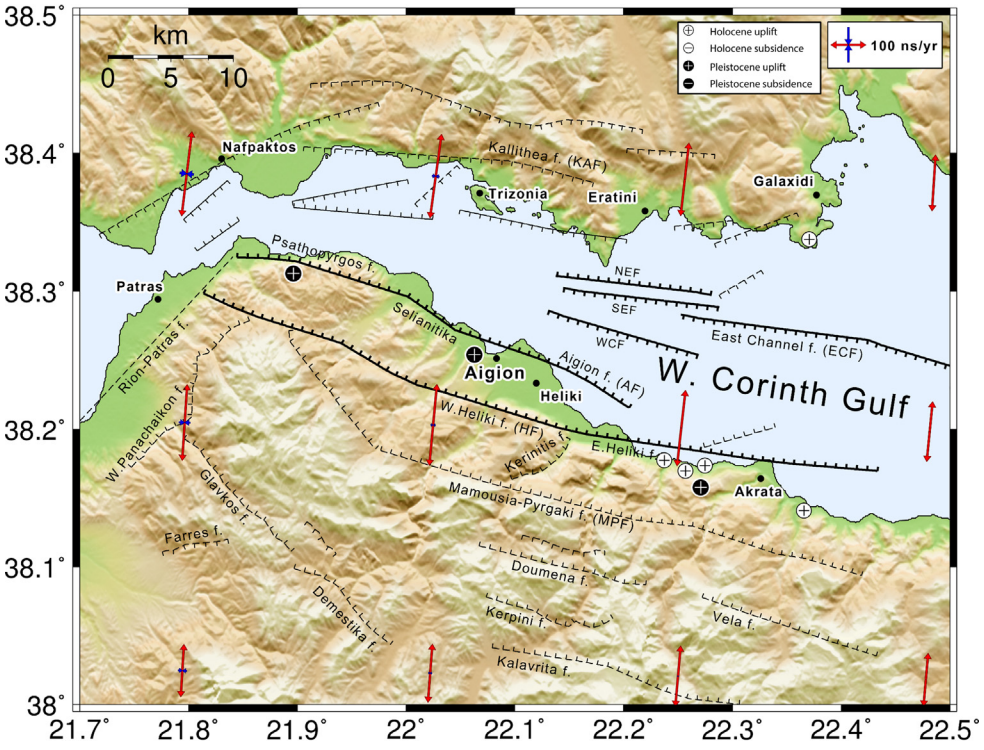

Fig. 2. Tectonic framework of the Aigion area. The onshore faults were provided by the KRIPIS research project and the faults offshore are after Bell et al. (2009). Double arrows denote the principal components of the strain tensor e_1 (in blue) and e_3 (in red), after Chousianitis et al. (2015). (For interpretation of the references to color in this figure legend, the reader is referred to the web version of this article.)

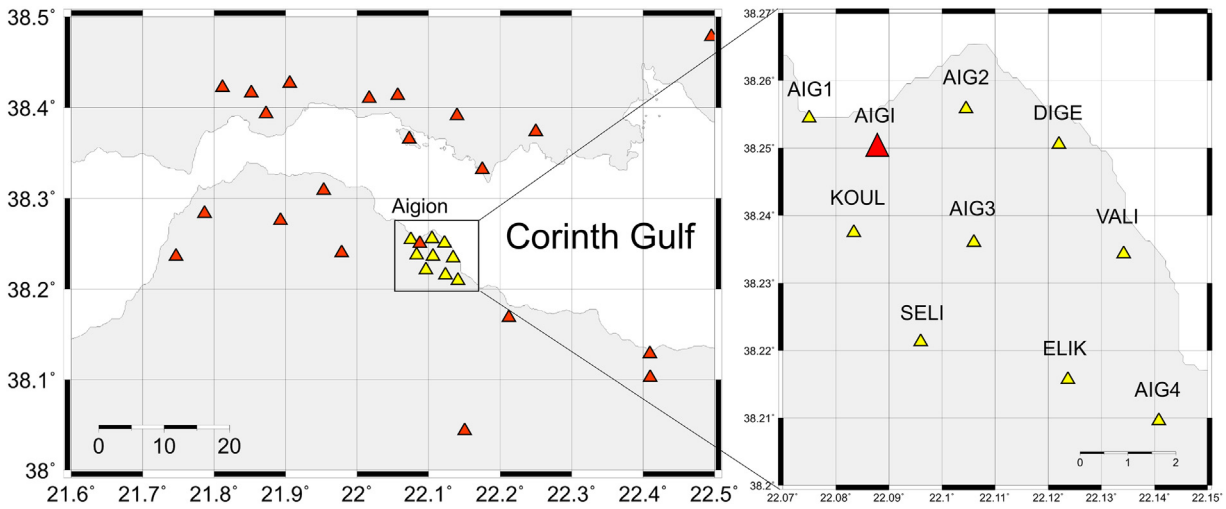

Fig. 3. Map of the seismological stations used in this study. Red solid triangles denote permanent stations. Yellow triangles denote stations of the temporary network. (For interpretation of the references to color in this figure legend, the reader is referred to the web version of this article.)

a detachment zone is indicated by geological data across the western part of the rift, which implies that the summed deformation due to the major faults is consistent with the measured geodetic rates. Therefore, a distributed deformation across isolated steeply dipping multiple faults has been suggested to explain the exhibited configuration (McNeill et al., 2005a; Bell et al., 2008, 2009).

A long history of large and catastrophic earthquakes occurred in the western part of the Corinth Rift near the city of Aigion and a plethora of references exist on the seismogenic processes of the region. The first bibliographic reference on the seismicity of this area is by Aristotle in his treatise of earth sciences titled 'Meteorologica' (350 B.C.), whereby he describes in detail the great 373 B.C. earthquake and the associated tsunami which destroyed the ancient city of Heliki. Since then, several large earthquakes have been reported for this area in: 23, 61, 1748, 1817, 1861, 1888, 1965 and 1995. Some of these large earthquakes as the 373 B.C, 1748, 1861 and 1995 have also generated tsunamis (Schmidt, 1879; Papazachos and Papazachou, 2003).

The largest recent earthquake in this area of magnitude Ms = 6.2, occurred on June 15th 1995 causing significant damage to the city of Aigion and 22 human casualties. This earthquake occurred on the northern shore of the Corinth Rift, across from the city of Aigion and has been associated with a north-dipping shallow fault (Bernard et al., 1997). This major earthquake gave rise to significant scientific interest for this area and since then, many collaborative projects have thoroughly investigated the western part of the Rift (Lyon-Caen et al., 2004; Bernard et al., 2006; Bourouis and Cornet, 2009).

On May 21st, 2013, a seismic sequence begun on the southern shore of the western part of the Corinth Rift, a few kilometers to the southeast of the city of Aigion. The sequence produced a cluster of more than 1500 recorded earthquakes with $0.4 \leq M_L \leq 3.7$ that caused cumulative structural damage mainly limited to old buildings. The largest event of the sequence with $M_L = 3.7$ occurred on May 31st, 2013. Shortly after the initiation of this activity, a dense local network of seismic stations was installed by the National Observatory of Athens (NOA) and the Seismological Laboratory of University of Athens (SLUoA), in order to improve the detectability of the Hellenic Unified Seismological Network (HUSN) (Mignan and Chouliaras, 2014).

In this investigation of the 2013 seismic sequence, we proceeded to analyze the waveform data by manually picking P- and S-wave arrival-times and calculated an optimum 1D velocity model that was subsequently considered in the relocation procedure. In addition, focal mechanisms using P-wave polarities were determined and were inverted to obtain the stress tensor and the stress field distribution. Further on, the existing spatiotemporal seismicity patterns of the sequence were investigated by the hydraulic diffusivity model (Shapiro et al., 1997), the Frequency-Magnitude Distribution (FMD) (Gutenberg and Richter, 1944), the Modified Omori Formula (MOF) (Utsu et al., 1995) and the Epidemic Type Aftershock Sequence (ETAS) model (Ogata, 1988).

2. Data analysis and results

Nine portable seismographic stations were installed shortly after the initiation of the seismic sequence on June 4th 2013 and remained in operation until September 3rd 2013 (Fig. 3). Five REFTEK-72A/24-bit and four Geotech-SMART24, digitizers equipped with 3 Lennartz LE3D/1 s, 4 Lennartz LE3D/20 s and 2 Guralp CMG40T/1 s seismometers, were appropriately installed with an average interstation spacing of ~2.3 km. The real-time data was transmitted to Athens by GPRS telemetry for online processing and archiving by the HUSN.

2.1. Waveform analysis

In total, more than 1500 earthquakes with an adequate signal-to-noise ratio and magnitudes $M_L = 0.4–3.7$ were detected during the recording period, providing for 22,120 P-wave and 15,260 S-wave arrival data.

The first step in the waveform analysis involved the accurate location of the events by the reduction of hypocentral uncertainties through the determination of an accurate velocity model for this area. We applied the method of Kissling et al. (1994) and the VELEST algorithm (Kissling, 1995), with input travel times calculated by the Hypoinverse procedure (Klein, 2000) using two suggested 1D velocity models for this area (Papadimitriou et al., 1994; Rigo et al., 1996). The resulting optimum velocity model and the respective hypocentral uncertainties are summarized in Tables 1a and 1b. The HypoDD relocation procedure (Waldhauser and Ellsworth, 2000, 2002) and the optimum velocity model of Table 1a were further employed in order to improve the hypocentral solutions, using phase and waveform data. Cross-correlation of the vertical components was performed using a nearest-neighbor linkage algorithm of the closest stations and events with similar waveforms were grouped together in multiplets, considering a threshold similarity value deduced from the empirical rule of Kapetanidis et al. (2010). In total 98% of events were successfully relocated with a

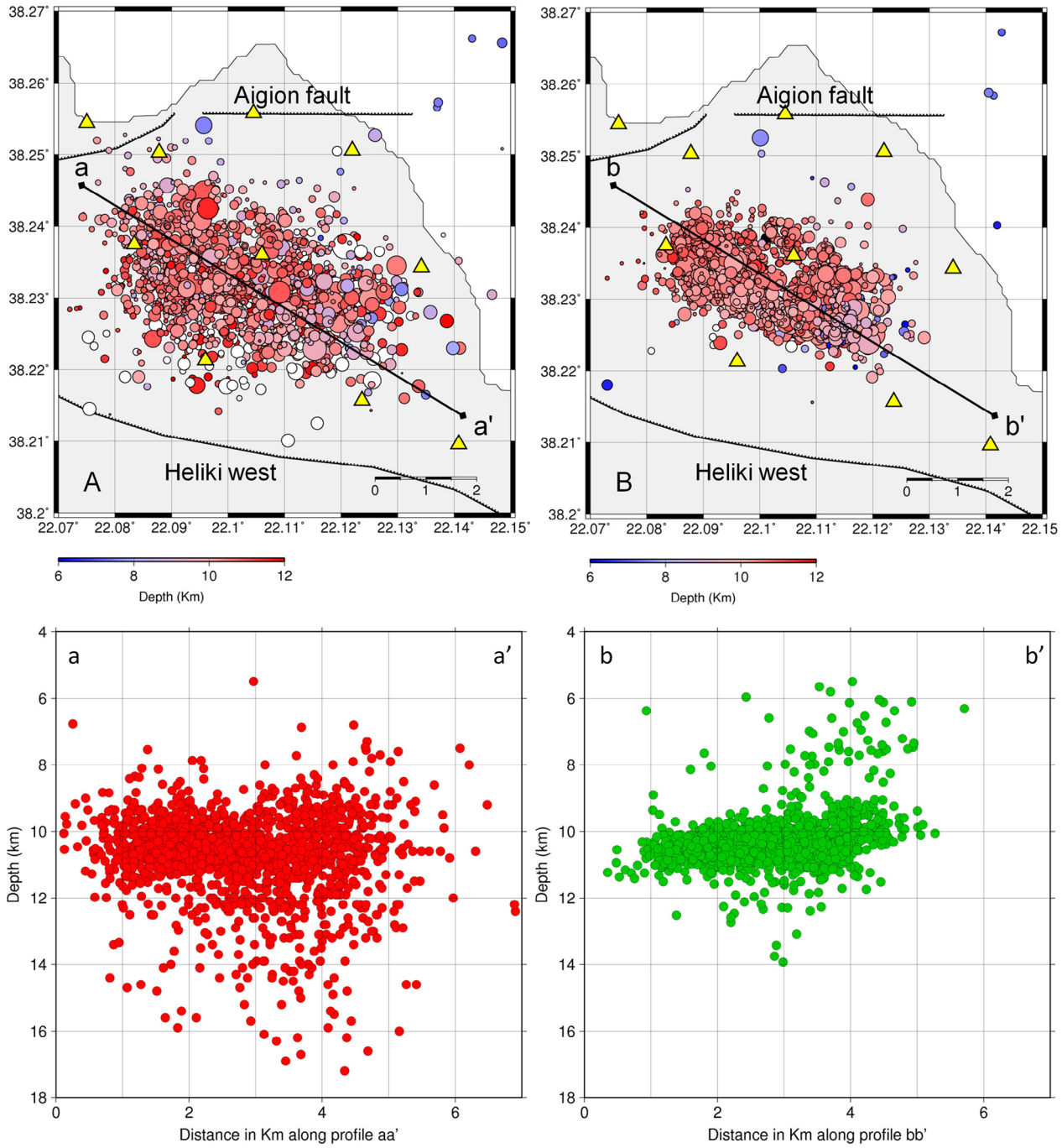

Fig. 4. Top: Spatial distribution of the 2013 cluster (A) located with Hypoinverse and (B) relocated with HypoDD. Bottom: vertical distribution of the seismicity along profiles aa′ and bb′ shown in panels A and B, respectively. Yellow triangles denote the stations of the temporary network. (For interpretation of the references to color in this figure legend, the reader is referred to the web version of this article.)

Table 1a
The proposed minimum 1D velocity model using two local velocity models (Papadimitriou et al., 1994; Rigo et al., 1996).

V_p/V_s	Papadimitriou et al. (1994)		This study	Rigo et al. (1996)		This study (final model)
Layer	1.84		1.80	1.80		1.73
	Ceiling depth (km)	P-wave velocity (km/s)	P-wave velocity (km/s)	Ceiling depth (km)	P-wave velocity (km/s)	P-wave velocity (km/s)
1	0	5.10	4.4	0.0	4.8	4.28
2	4	5.80	5.87	4.0	5.2	4.52
3	12	6.10	6.11	7.2	5.8	5.55
4	30	7.30	7.26	8.2	6.1	6.01
5				10.4	6.3	6.35
6				15.0	6.5	6.54
7				30.0	7.0	7.02

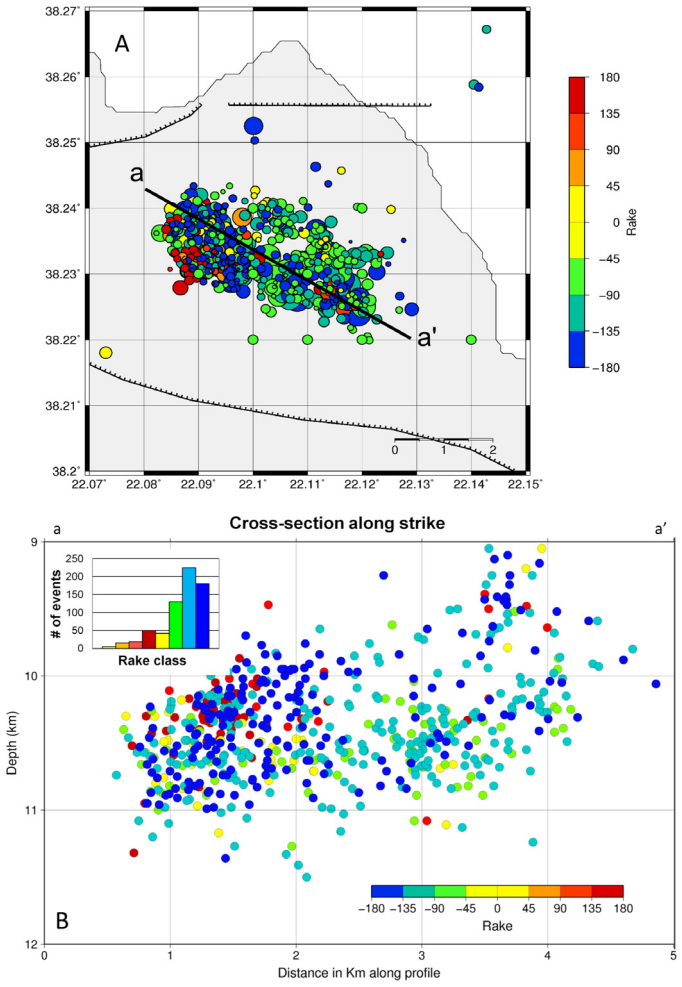

Fig. 5. (A) Map of relocated hypocenters for which focal mechanisms were computed, color coded by the faulting type, according to Zoback's (1992) classification scheme. (B) Vertical distribution of the faulting types along aa′ profile shown in panel A. The embedded histogram in panel B shows the multitude of each faulting type.

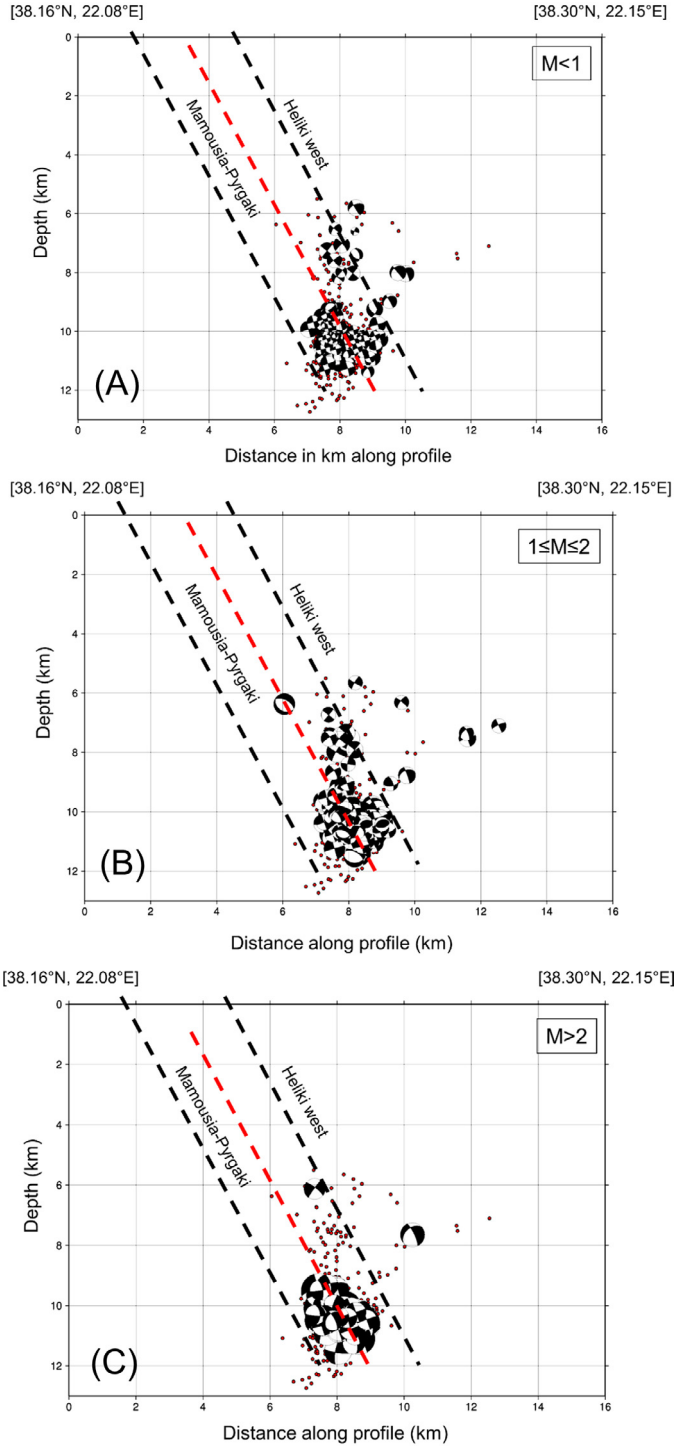

Fig. 6. Vertical cross-sections along a N20° profile including hypocenters and focal mechanisms for events classified into three magnitude ranges: (A) $M_L < 1$, (B) $1 \le M_L \le 2$, (C) $M_L > 2$. Black dashed lines denote active faults observed at the surface that have been projected in depth with a dip of 60°. The red dashed line denotes the inferred activated seismogenic zone. (For interpretation of the references to color in this figure legend, the reader is referred to the web version of this article.)

spatial uncertainty in their relative locations of the order of a few tens of meters. The HypoDD results demonstrate significant clustering of the seismic events when compared to those obtained by the Hypoinverse procedure. This spatial confinement of the swarm is observed onshore, in a volume with dimensions $\sim 4 \times 2 \times 6\,km^3$, striking ~N110° and at a depth range between 6 and 12 km (Fig. 4).

Subsequent to the relocation procedure, we proceeded to determine 666 fault plane solutions using the recorded P-wave first-motion polarities. In addition to the data from the portable seismic network, we also incorporated measurements from the HUSN stations and our solutions were constrained by at least 10 P-wave polarities. This analysis resolved the nodal planes of the focal mechanisms with an uncertainty of less than 10°. Fig. 5A and B presents the spatial distribution of the focal mechanisms in the planar and cross-section view, respectively, using to the classification of Zoback (1992). These results demonstrate that normal faulting mainly dominates in the entire seismogenic volume. In addition to this, we also observe another significant sample of events located at the western part of the seismogenic zone, which is found to exhibit oblique slip and reverse faulting. Overall, the average focal mechanism for the area indicates the nodal plane strikes to be N88° and N287° with average dip values of 32° and 61°, respectively.

Cross-sections in a N20° direction, perpendicular to the inferred strike of the seismogenic zone, depict a simple geometry, consisting of north-dipping planar faults with an average dip of ~60°, at depths between 6 and 12 km (Fig. 6). This geometry is compatible with the activation of the network of minor normal faults located in-between the Pyrgaki-Mamousia and Heliki faults as suggested by Moretti et al. (2003). In Fig. 6A–C we note a possible activation of the Heliki fault at a depth between 6 and 8 km

Table 1b
Summary of location errors for the models of this table.

Location error	Dataset C			
	Papadimitriou et al. (1994)	This study	Rigo et al. (1996)	This study
Mean RMS (s)	0.16	0.15	0.14	0.14
Median RMS (s)	0.16	0.15	0.14	0.13
Mean ERH (km)	0.70	0.68	0.69	0.67
Median ERH (km)	0.70	0.65	0.70	0.60
Mean ERZ (km)	0.65	0.67	0.63	0.63
Median ERZ (km)	0.60	0.60	0.60	0.60

for several events, with no evidence for activity on the Pyrgaki-Mamousia fault.

2.2. Stress inversion

Using the computed focal mechanisms of the 2013 sequence and data from a similar sequence which occurred in this area in 1991 (Papadimitriou et al., 1994), we performed a Formal Stress Inversion (FSI) using the MSATSI algorithm (Hardebeck and Michael, 2006; Martínez-Garzón et al., 2014). The combination of these two datasets provided 826 focal mechanisms for the inversion and the results are presented in Appendix A and in Fig. A1. Overall the inversion results indicate a rather homogeneous stress field and it is further observed that: the σ_3/*T*-axis is almost horizontal, indicating extension in N5° direction, the σ_1/P-axis indicating almost vertical compression and the intermediate σ_2/B-axis is found to have a strike N95° with a plunge of W15°.

Further on, the spatial stress distribution was mapped by the 2D FSI method. The study area was divided in 60 equal rectangles with dimensions 0.005° × 0.005° (Fig. A2 in Appendix A) and the inversion was performed using at least 10 focal mechanisms for each rectangle, by adopting solutions lying within the 95% confidence interval as determined by the bootstrapping method (Hardebeck and Michael, 2006). These results are presented in Fig. 7 whereby Fig. 7A and C shows a dominant normal type of faulting with a horizontal σ_3 component (*T*-axis) and a nearly vertical P-axis for the majority of the grid points. This is consistent with the focal mechanism pattern which was described earlier and also shows a significant heterogeneity at the western part of the activated zone. This heterogeneity is as expressed by the variance of the orientation and plunge of the σ_1 and σ_2 components (P- and B-axes, respectively) and also by the lower values of *R* (stress ratio), which are different in the western part of the seismogenic area in comparison to the eastern part as presented in Fig. 7B and D. In addition it is found that the 1991 and 2013 seismic activities have provided similar results regarding the heterogeneity across the western part of the fault zone.

2.3. Spatiotemporal patterns

The time histogram of Fig. 8A demonstrates the presence of the two seismicity phases A and B. Phase A, from May 21st until July

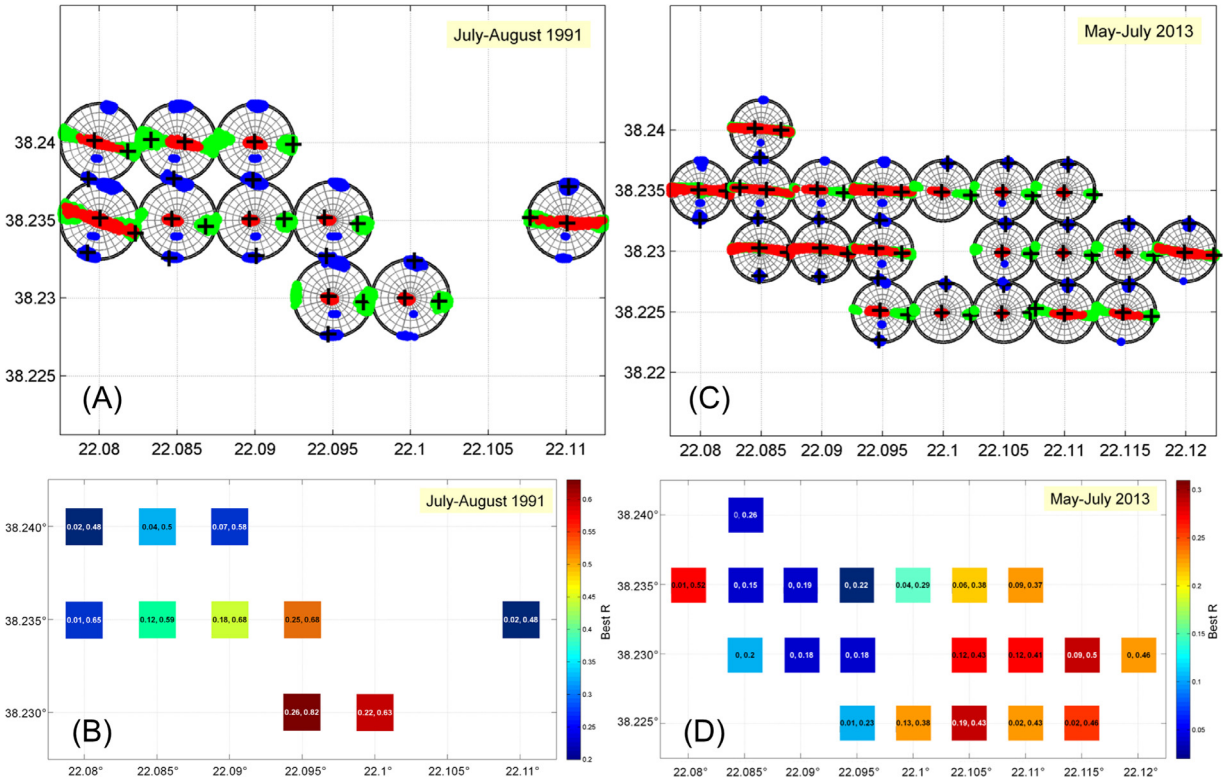

Fig. 7. (A, C) Results of the 2D inversion for the 1991 and the 2013 data, respectively. Red, σ_1; Green, σ_2; Blue, σ_3; Black cross: best solution; Colored dots: solutions within the 95% confidence level. (B, D): Maps of the stress ratio (*R*) values corresponding to the stereomaps of the top panel for the 1991 and the 2013 data, respectively. The best solution for each grid point appears as color encoded rectangle, whereas the uncertainty interval is shown within it. (For interpretation of the references to color in this figure legend, the reader is referred to the web version of this article.)

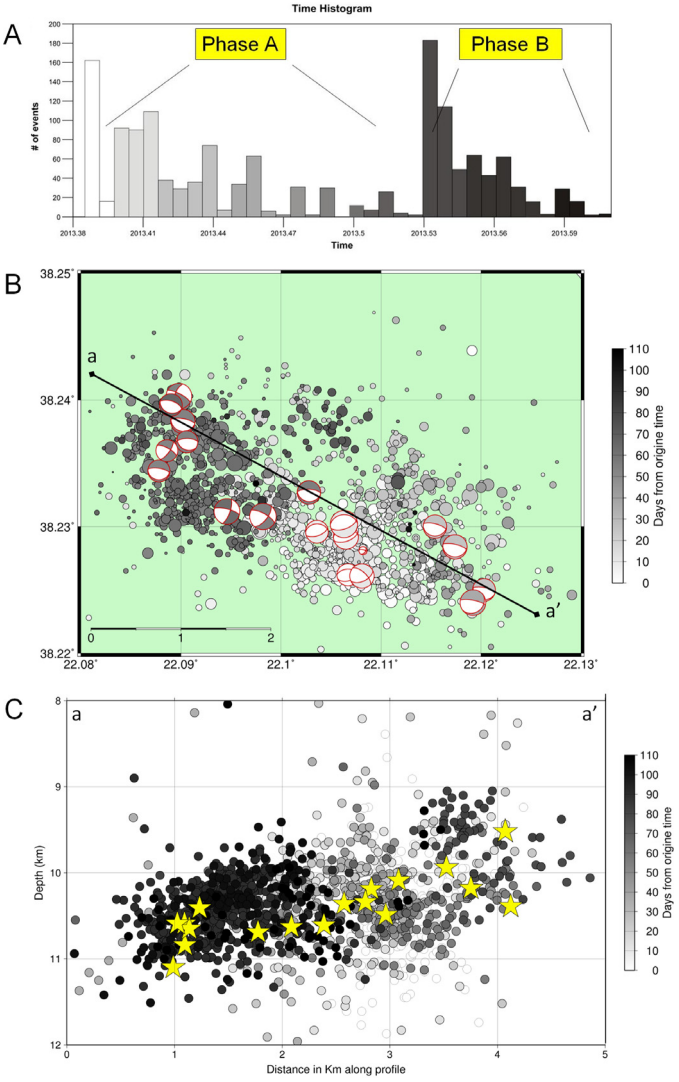

Fig. 8. (A) Histogram of the temporal evolution of the seismic swarm activity with respect to the multitude of the events, where several temporal clusters are distinguished. (B) Spatiotemporal distribution of the seismic activity and focal mechanisms for events with $M_L \geq 3$. The line aa′ drawn in N110° direction is used for the cross-section of panel C and the spatiotemporal projection of Fig. B1. (C) Cross-section along aa′ profile showing the temporal distribution of the seismic activity. The time progress is presented in grayscale, from white for the beginning to black for the end of the activity. Stars denote events with $M_L > 3$.

12th (2013.382–2013.529) and Phase B, from July 13th until the end of August (2013.530–2013.675). The main peaks of seismicity for each phase are found to occur on May 21st–22nd (2013.285) with 160 seismic events and July 13th–14th (2013.53) with 280 events, respectively. Following this, we use a gray scale to express the number of days since the initiation of the seismic activity (May 21st) and in Fig. 8B and C we map the spatial and temporal variation of the seismic activity in planar and in a cross-sectional view, respectively. These results clearly indicate that the seismic activity was initiated in phase A at the eastern part of the seismogenic zone (lighter gray) and migrated westwards where it is found to be entirely confined in phase B (darker gray).

The temporal evolution of the seismicity and also the temporal evolution of the focal mechanisms and their respective stress field variance of the 2013 sequence are examined in Fig. 9. We have used the ZMAP software (Wiemer, 2001), for overlapping time windows, each containing 100 samples and plotted the temporal evolution of the 2013 cumulative seismicity (black curve) and the stress field variance (blue curve) obtained by the focal mechanism inversion. From this result it is clearly observed that that the largest stress variance of the order of 14%, corresponds to the intermediate period (2013.53) between phase A and B. A secondary peak of 12% variance is also observed toward the middle of phase B (2013.57), just prior to the decrease in the cumulative seismicity. The focal mechanisms of the largest events with $M_L > 3$ are shown to exhibit a homogeneous pattern of ~E–W normal faulting during phase A, while phase B is found to exhibit an inhomogeneous pattern.

Results from the statistical analysis of earthquake catalogs and laboratory experiments have demonstrated that the slope of the frequency-magnitude distribution of the Gutenberg and Richter (1944) law, namely the "*b*-value", is inversely proportional to the applied stress while on a larger scale the *b*-value is a constant, approaching the value of 1 (Kagan, 1999; Schorlemmer et al., 2005; Goebel et al., 2013). It has also been demonstrated that prior to large earthquakes the *b*-value decreases because of the increase in confining pressure. In volcanic swarms and aftershock sequences the *b*-values are higher because of the high heterogeneity of smaller fractures, and in intraplate seismic swarms the *b*-values are lower as a result of the increase in the pore pressure due to crustal fluid intrusion (Hainzl and Ogata, 2005; Ibs-von Seht et al., 2008; Nanjo et al., 2012). The majority of the above-mentioned temporal seismicity patterns and results have produced a variety of scaling relationships such as the Frequency-Magnitude Distribution (FMD), the Modified Omori Formula (MOF) and the Epidemic Type Aftershock Sequence model (ETAS), in order to detect and identify temporal variations of seismicity associated with different physical processes in the Earth's crust (Ishimoto and Iida, 1939; Ogata, 1988; Utsu et al., 1995).

As mentioned previously, the Aigion seismic sequence in 2013 produced a catalog of 1500 events with $M_L = 0.4–3.7$, from May 21st until September 3rd, 2013. This earthquake catalog is analyzed with the ZMAP software (Weimer, 2001) to determine the temporal variation of the FMD, the MOF and the ETAS model parameters. Fig. 11A shows the FMD and its first derivative (upper and lower curves, respectively) whereby the crosshair at the derivative maximum indicates the catalog's homogeneity, expressed as the magnitude of completeness (Mc), as defined by Wiemer and Wyss (2000). Our data indicate an Mc = 1.1 which is a significant improvement in the detectability for seismic events due to the installation of the additional local network, when compared to the Mc ~2.5–3, derived from the HUSN network distribution of permanent seismic stations in the broader region (Mignan and Chouliaras, 2014). Further on the slope of the FMD is determined by the weighted least squares method (dashed line), indicating a rather low *b*-value = 0.85 (±0.03).

Using Mc = 1.1 as a lower magnitude threshold and starting from May 21st, the cumulative and non-cumulative time series for the first 80 days of the seismic sequence are presented in Fig. 10B. Two distinct phases are clearly identified, whereby the first phase A is characterized by a ~50 day stepwise pattern of successive quiescence/activation sub-periods, followed by the second phase B which was initiated on July 13th and is shown to produce a smoother pattern of energy release. The two phases identified by the two different seismicity patterns are also evident when comparing their respective FMD and *b*-values in Fig. 10C and D, whereby a *b*-value = 0.89 is determined for the first phase (A) and a *b* = 0.77 is determined for the second phase (B). In view of the inverse relation of the b-value to the stress level (Schorlemmer et al., 2005; Goebel et al., 2013), the decrease in the *b*-values between the two phases indicates an increase in stress and a migration from a low stress (higher *b*-values) in phase A to a higher stress (lower *b*-values) in phase B.

Next in our temporal analysis, we employ the SASeis software in which a likelihood maximization of the MOF and the ETAS model

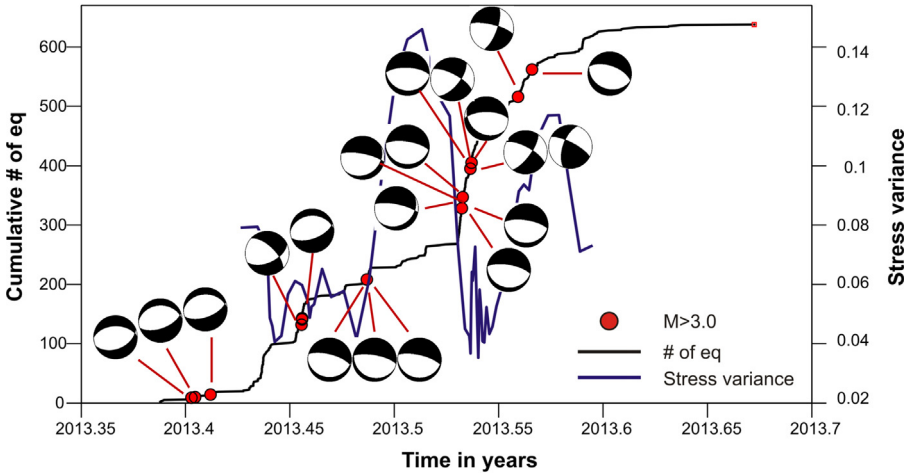

Fig. 9. Diagram presenting the temporal distribution of the seismic sequence and the stress field variance. Focal mechanisms correspond to events with $M_L > 3$.

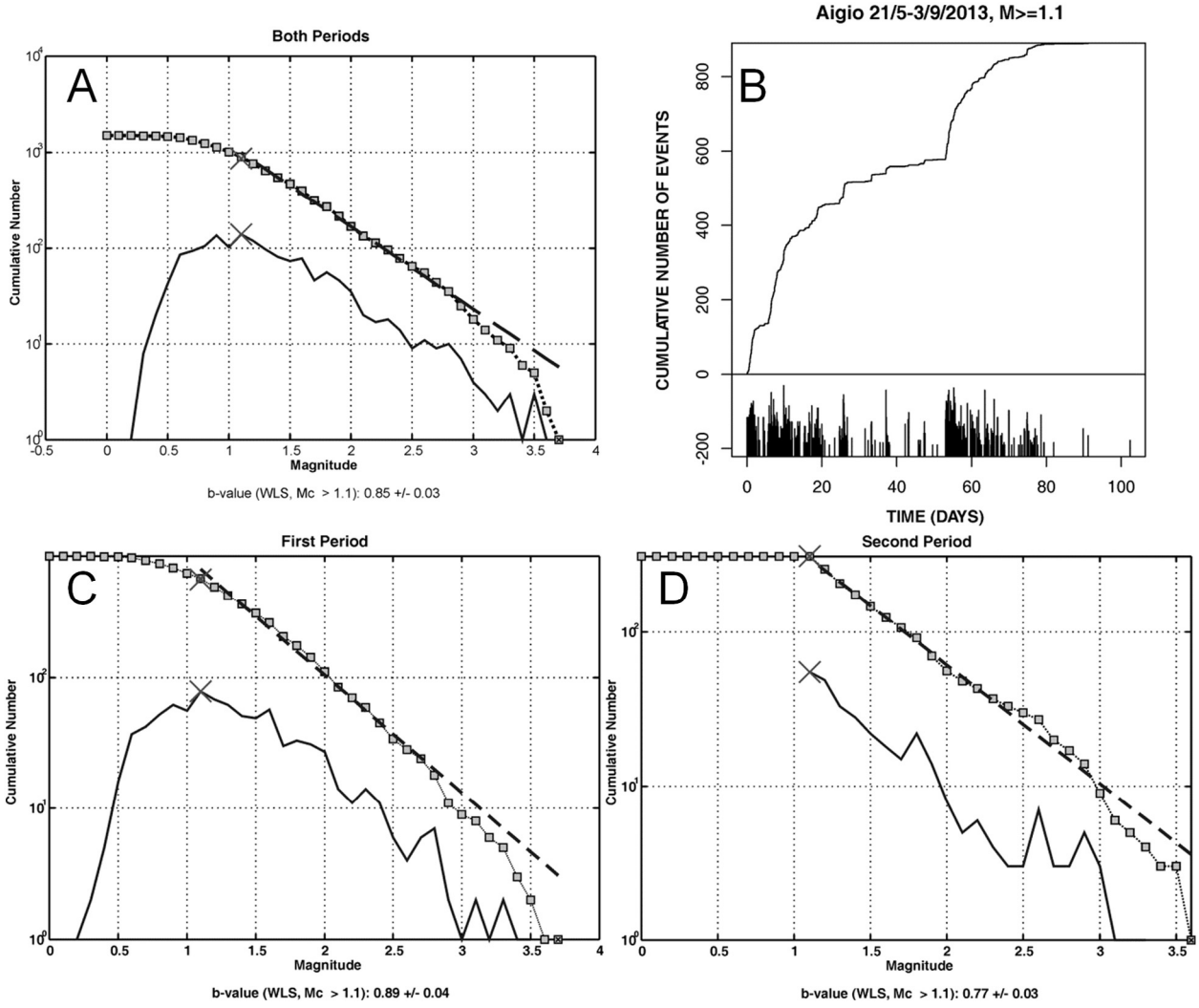

Fig. 10. (A) FMD and its first derivative (upper and lower curves, respectively) for the entire catalog of this study. The crosshair at the derivative maximum indicates the Mc = 1.1 value. A *b*-value of 0.85 (±0.03) is determined with the weighted least squares method (dashed line). (B) Cumulative and non-cumulative time series for the first 80 days of the seismicity sequence using a Mc = 1.1 as a lower magnitude threshold. Differences in the seismicity rates between (C) FMD for the first period and (D) FMD for the second period. Both periods are examined with Mc ≥ 1.1 and the *b*-values are determined with the weighted least squares method.

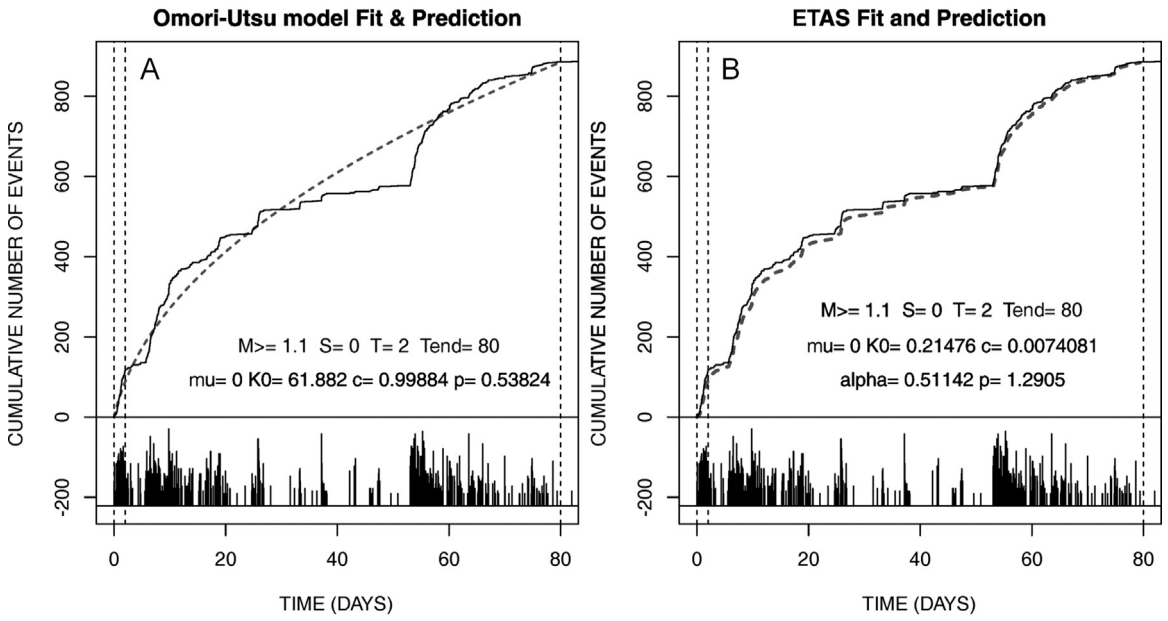

Fig. 11. (A) MOF and (B) ETAS results, taking into account the entire seismic sequence with Mc ≥ 1.1. The black line indicates the cumulative number of seismic events and the red line indicates the model's fit and prediction. The first and second dotted lines represent the modeling fitting period (T = 2 days) while model's prediction period is between the second and third dotted lines. (For interpretation of the references to color in this figure legend, the reader is referred to the web version of this article.)

parameters is performed (Utsu and Ogata, 1997). Since we have identified two different phases of seismic activity in the 2013 sequence, we have produced MOF and ETAS fit and prediction models for the entire sequence in Fig. 11 as well as for each phase separately in Fig. 12.

Fig 11A and B presents the MOF and ETAS results respectively, taking into account the entire seismic sequence. The black line indicates the cumulative number of seismic events and the dashed line indicates the model's fit and prediction. We point out that $mu = 0$ has been chosen because we assume that the background seismic activity is null in the short period that is considered and that the stress field change is due to the largest (M_L = 3.7) shock near the beginning of the sequence. The first and second dotted lines, perpendicular to the time axis, represent the modeling fitting period (T = 2 days), while the model's prediction period is between the second and third dotted lines. A comparison of the two figures indicates a poor fit of the Omori-Utsu model in Fig. 11A while the ETAS model in Fig. 11B is found to predict the entire sequence more accurately.

Separate MOF and ETAS model results for the first period (phase A) and second period (phase B) phases are presented in Fig 12A–D, respectively. A comparison of the results from the first period (phase A) starting on May 21st, indicates a poor fit of the Omori-Utsu model (Fig. 12A) while the ETAS model (Fig. 12B) is found to provide a more accurate prediction. In contrast to this, for the second period (phase B), starting on July 13th, a better fit of the Omori-Utsu model is obtained (Fig. 12C), while the ETAS model (Fig. 12D) is found to have a poorer fit.

Interestingly, the alpha value = 0.48 which is a measure of the efficiency of a shock in generating an aftershock activity relative to its magnitude (Ogata and Zhuang, 2006), is within the range 0.35–0.85 that has been observed in earthquake swarm activity associated with a fluid driven mechanism in Japan (Ogata, 1992) and Vogtland/NW Bohemia (Hainzl and Ogata, 2005), while non-swarm activity is generally characterized by higher alpha values, in the range 1.2–3.1.

We consider the possibility for a fluid driven mechanism for the 2013 sequence and this issue is further investigated with the approach of Shapiro et al. (1997) through the spatiotemporal analysis presented in Appendix B. The envelopes in Fig. B1 correspond to the distance of the seismicity front relative to the two phase (A and B) initiation times (May 21st for phase A and July 13th for phase B), assuming a hydraulic diffusivity of 0.21 $m^2 s^{-1}$ and 0.196 $m^2 s^{-1}$, respectively. These hydraulic diffusivity values are compatible with the ones found by Pacchiani and Lyon-Caen (2010) who proposed a fluid driven causative mechanism to explain the pattern of upward migration of seismicity that was observed during the seismicity swarm in 2001, which took place ~3–4 km south of the city of Aigion.

The Aigion Municipal Authority provided us with geochemical data for the 2013 sequence as described in Appendix B. In Fig. B2 we observe a systematic decrease of the acidity indices (pH values) of table water samplings from 2 aquifers before the 2013 seismic swarm. Unfortunately the sampling frequency of the acidity indices could not provide us with more detailed results during the 2013 sequence, however we point out that in a previous study from a nearby borehole (AIG-10), Doan and Cornet (2007) interpreted thermal anomalies as the interaction of meteoric water circulating through the area's normal faults with a high thermal field.

3. Discussion

In view of the large and catastrophic earthquakes that have occurred in the past, the Corinth Rift has been the site of many scientific investigations and comprises a 'natural' laboratory for geoscientists. Within this context, we studied the most recent seismic crisis which occurred in this region during May–July 2013. This sequence did not produce a large main shock but rather more than 1500 events of small magnitudes ($0.4 \leq M_L \leq 3.7$) during its three-month duration. Shortly after the initiation of the sequence, a dense network of 9 local seismic stations was installed in the immediate area, significantly enhancing the detection of seismic events and lowering the magnitude of completeness to Mc = 1.1 compared to the previous Mc 2.5–3 for this area, as determined by Mignan and Chouliaras (2014) for the HUSN network of permanent seismic stations. This detection increase mainly involving small magnitude events has provided a valuable data set to investigate in this study the associated seismotectonics and the spatiotemporal seismicity

patterns in order to provide insight regarding the possible physical mechanism that triggered the 2013 seismic sequence.

Robust analyses using the waveform dataset recorded by the HUSN and the local network demonstrate that the 2013 seismogenic zone involves a rather small seismogenic volume ($\sim 4 \times 2 \times 6\,km^3$) comprised of 60° north-dipping normal faulting striking in a N110° direction, located on the southern shore of the Corinth Rift at a depth range ~6–12 km (Fig. 13). The fault plane geometry and the resulting stress tensor inversion indicates a predominant N5° horizontal extension in agreement with the observed strain from GPS results (Clarke et al., 1998; Briole et al., 2000; Avallone et al., 2004) capable of producing according to orthogonality dip slip normal faulting that strikes in a N275° direction. (Micarelli et al., 2003; Moretti et al., 2003; McNeill et al., 2005a; Bell et al., 2008).

The north-dipping nodal planes of the 826 focal mechanisms used in this study have an average strike of N287°, a value that is compatible with the major faults direction across the western part of the rift and also consistent with extension obliquity of $\alpha = 12°$, which represents orthogonal/low obliquity rifting.

No evidence for a shallow-dipping seismicity zone is revealed by our results and no earthquake is observed at the uppermost part of the crust, in agreement with Rigo et al. (1996), Bernard et al. (2006) and Lambotte et al. (2014). Onshore, the upper limit of the seismogenic layer is observed ~1–2 km deeper than offshore. The alignment of hypocenters and the arrangement of the nodal planes of the determined focal mechanisms do not show the presence of a major detachment fault in the area of our investigations.

The faulting pattern in Fig. 13 fits the geometry of the seismicity clusters and the onshore seismicity distribution of the 1991

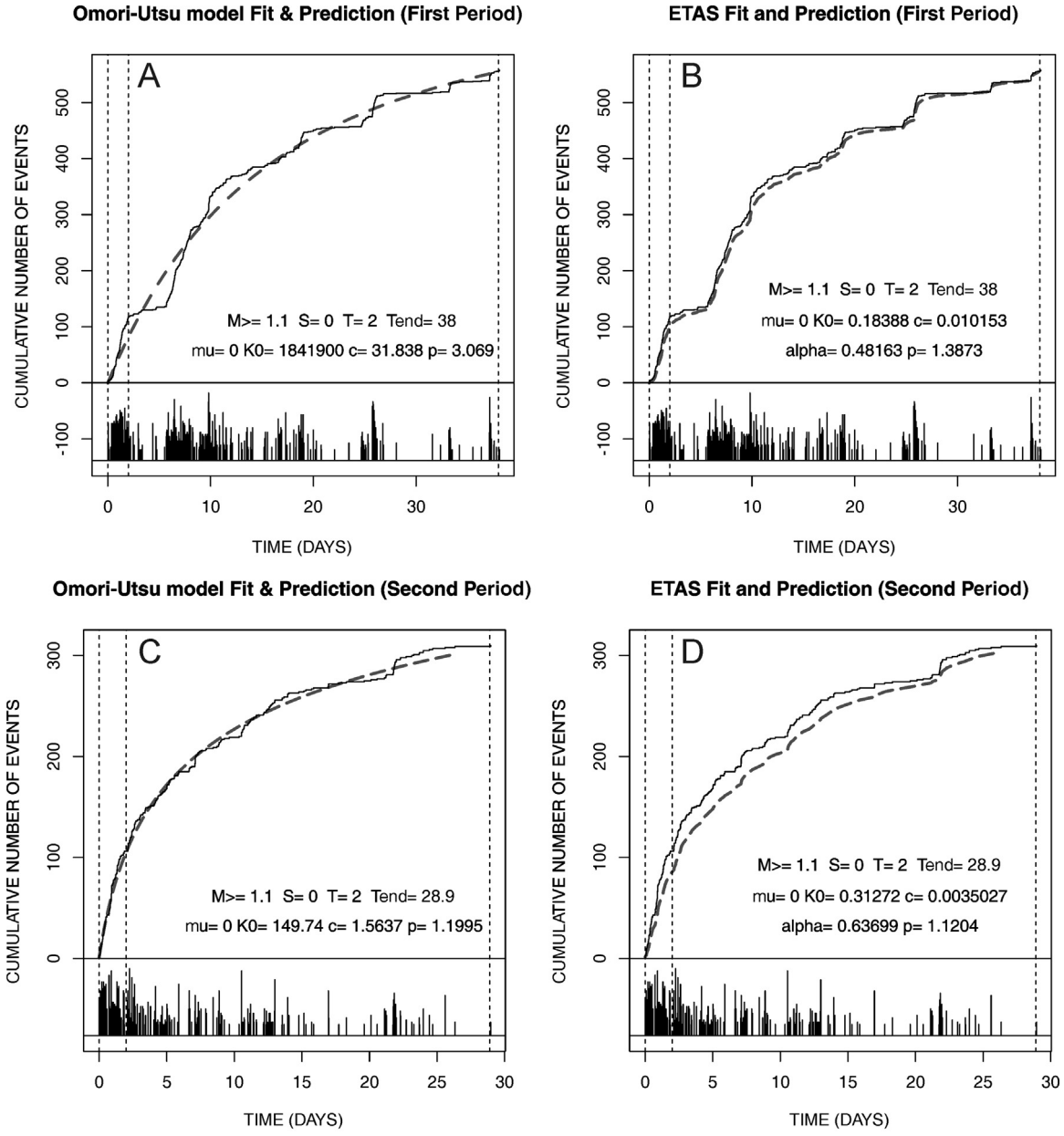

Fig. 12. (A) MOF and (B) ETAS results, for the first period of the seismic sequence (C) MOF and (D) ETAS results, for the second period of the seismic sequence with Mc ≥ 1.1. The black line indicates the cumulative number of seismic events and the dashed line indicates the model's fit and prediction. The first and second dotted lines represent the modeling fitting period ($T = 2$ days) while model's prediction period is between the second and third dotted lines.

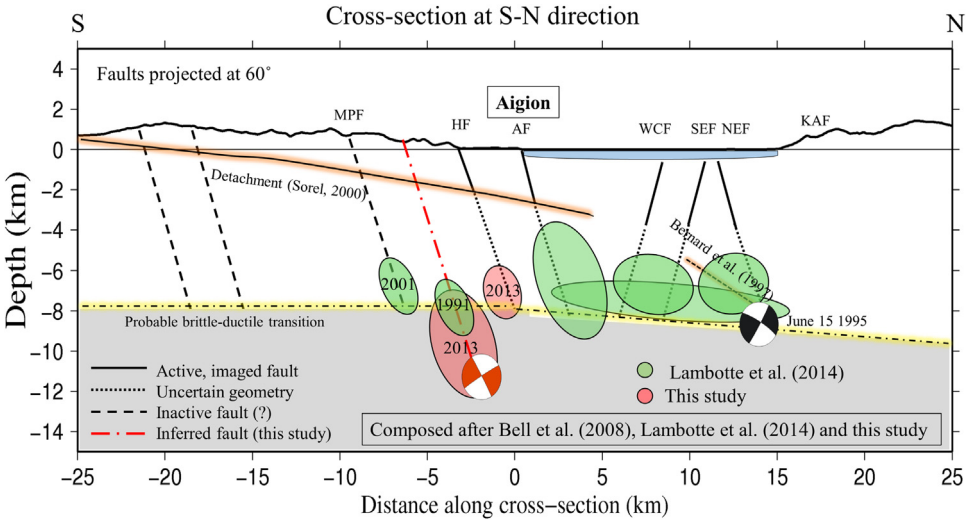

Fig. 13. Cross-section in S-N direction, centered at 38.25° N, 22.08° E, presenting the geometry of major faults in the western Corinth Rift. Onshore (Collier and Jones, 2003) and offshore faults (Bell et al., 2008) have been projected with dips of 60° down to the probable depth of the brittle-ductile transition. The detachment surface proposed by Sorel (2000) is also projected. Red and green ellipses denote the inferred configuration of reliable seismicity clusters from this study and Lambotte et al. (2014), respectively. MPF: Mamousia-Pyrgaki Fault; HF: Heliki Fault; AF: Aigion Fault; WCF: Western Channel Fault; SEF: South Eratini Fault; NEF: North Eratini Fault. (For interpretation of the references to color in this figure legend, the reader is referred to the web version of this article.)

(Rigo et al., 1996), the 2001 (Lyon-Caen et al., 2004) and the 2013 seismicity sequences. An offshore deep seismicity cluster aligned in a sub-horizontal sense is likely correlated with the lower seismicity cut-off boundary, rather than a shallow dipping fault as suggested by Taylor et al. (2011). These results are also in agreement with Hatzfeld et al. (2000) who attribute the seismicity in the western Corinth Rift to the interaction between steeply dipping antithetic faults interacting with the brittle-ductile transition zone. This faulting geometry supports the observed northward tilt of basin sediments (De Martini et al., 2004) and it is further compatible with findings from high-resolution seismic reflection and multi-beam bathymetric data (McNeill et al., 2005a; Bell et al., 2008, 2009).

Lithospheric-scale analog models of continental extension, verified for the Western and Eastern branches of the East African Rift, have suggested a two-stage deformation, whereby fault-bounded basins in an initial stage of rifting evolve in a later stage to regions of faulting and lithospheric thinning within the rift floor, with trend, architecture and kinematics controlled by the angle of rifting with respect to the extension axis (Corti, 2012). Similar results concerning a two-stage deformation pattern were also derived by numerical modeling (Van Wijk, 2005). Ziegler and Cloetingh (2004) describe a typical evolution of narrow orthogonal continental rifts in the Main Ethiopian Rift (Corti, 2009), as systems of long faults showing almost pure dip-slip displacement, perpendicular to the regional extension and often having large vertical throw. Progressive deformation is suggested to lead to faulting migration from the rift boundaries to the rift floor with the activation of new high-angle normal faults, whereas boundary faults are progressively deactivated. This is the case for the southern marginal faults of Mamousia-Pyrgaki fault (Doumena, Kerpini) (Fig. 2) which produced an impressive relief south of Aigion and presently they are considered inactive (e.g. Collier and Jones, 2003).

Due to low obliquity ($15^\circ \leq \alpha \leq 45^\circ$), narrow rifting deformation in the upper crust responds to both the far-field extension direction and the local stress reorientation imposed by the obliquity of the weak zone, resulting in *en echelon*, oblique boundary faults that follow the trend of the weak zone. This configuration is compatible with *en echelon* faults in the southern margin of the Corinth Rift. A possible assumption to explain these *en echelon* faults is the obliquity increase to the east, which is an intriguing aspect for future research in the presence of data availability. In view of the above, we suggest that the geometry and kinematics of typical, narrow, almost orthogonal rifting, inferred from the stress inversion, explains our implications for steeply dipping normal faults down to the depth of the brittle-ductile zone and that detachment zones proposed for the area are unlikely to exist. Such an arrangement can likely be explained by a continuum flow in brittle-ductile rheology because of which the development of normal faults along detachments does not require listric faulting (Neumann and Zuber, 1995).

The statistical analysis of the 2013 sequence using 1500 events of small magnitudes ($0.4 \leq M_L \leq 3.7$) has provided interesting results concerning the spatial and temporal patterns that have emerged by the use of different methods. The presence of two separate seismicity phases in time and also in space, to the eastern and the western parts of the seismicity cluster, have been analyzed.

The 2013 seismic sequence began on the eastern part of the seismogenic zone, with normal faulting and a burst-type seismicity phase. After a brief period of quiescence, a second seismicity phase started in the western part of the zone, involving mainly normal but also strike-slip and reverse faulting as well. The quiescence period between the two cycles exhibits a large variance in the stress field, possibly indicates different physical mechanisms for the two phases.

The difference in the stress patterns of the two phases is also reflected in the different results in the FMD, MOF and ETAS models associated with each of the two phases that compose the 2013 seismicity cluster. In view of the inverse relationship between stress and the *b*-value, the results of this study show that the 2013 seismicity migrated from a low-stress zone with relatively larger *b*-values ($b = 0.89$) in the east during phase A to a high-stress zone of lower *b*-values ($b = 0.77$) to the west in phase B. Such a pattern can be related to triggering by fluids diffusion (Hainzl and Ogata, 2005) and/or the evolution of the Rift from east to west, in agreement with Armijo et al. (1996), Clarke et al. (1998), Nyst and Thatcher (2004).

The burst type of seismicity of the first phase is best modeled with the epidemic transfer of stress according to the ETAS model. The determined alpha value, which is a measure of the efficiency of a shock in generating an aftershock activity relative to its magnitude has a low value (0.48) characteristic of 'swarm' activity, in contrast to higher alpha values produced by non-swarm activity

in the range 1.2–3.1 (Hainzl and Ogata, 2005, Ogata, 1992). To the contrary, the second phase is best-modeled with the MOF decay law, indicating that the activity is mainly generated by the stronger events at the beginning of the phase.

The overall low *b*-value (<1) and ETAS prediction model of the 2013 sequence indicate high and localized stress, which is a known factor responsible for the generation of earthquake swarms (Mogi, 1963) as well as epidemic transfer of energy. Similarily low *b*-values have also been observed in other earthquake swarms in continental rifts (Ibs-von Seht et al., 2008).

It has been proposed that microearthquakes can be triggered along pre-existing fault zones by small increases in pore pressure especially at depths approaching the brittle-ductile transition (Zoback and Harjes, 1997). Recent seismicity sequences at the Corinth Rift without a large main shock, namely 'seismicity swarms', have been proposed to be driven by such a fluid diffusion model (Bourouis and Cornet, 2009; Pacchiani and Lyon-Caen, 2010).

4. Conclusions

A detailed seismotectonic study of a seismicity sequence composed of 1500 small earthquakes with ($M_L \leq 3.7$) that occurred in 2013, onshore in the southwestern coast of the Corinth Rift is presented. Robust hypocentral solutions and reliable focal mechanisms imply for the activation of a seismogenic zone of dimensions of $\sim 4 \times 2 \times 6\,km^3$ that lies at a depth range between 6 and 12 km, on a N110° striking and 60° north-dipping normal fault, located between the Mamousia-Pirgaki and Heliki faults. Two clusters of seismicity are distinguished and a westward epicentral migration is demonstrated, from a region of low stress to a region of high stress. During this process, a significant variance in the stress field is observed with a homogeneous stress field in the eastern part of the cluster and an inhomogeneous field to the western part of the cluster. Overall, the exhibited low *b*-values are attributed to high stresses while the sequence may be best modeled by the epidemic transfer of stresses described by the ETAS model. The involvement of fluids in this particular process, although considered, could not be adequately resolved.

Acknowledgements

The authors would like to thank the Aigion municipality authorities and I. Karagiannopoulos, S. Liakopoulos for their valuable help during the installation and maintenance of the local network. In addition we thank the two reviewers and the Editor of the Journal of Geodynamics for their constructive comments during the review process. The active fault data were provided by the GSRT research project "Infrastructure Upgrade for Seismic Protection of the Country and Strengthen Service Excellence through Action", project MIS-448326, implemented under the Action "Development Proposals for Research Bodies-KRIPIS".

Appendix A.

A.1. Stress inversion

A Formal Stress Inversion (FSI) (Hardebeck and Michael, 2006) of 826 focal mechanisms concerning the 1991 and 2013 seismic sequences has been performed using the MSATSI algorithm (Martínez-Garzón et al., 2014). The stereonets presented in Fig. A1 indicate the lower hemisphere projection of the inverted principal stress components. A 2D FSI was performed to determine the spatial distribution of the best-fit stress tensor within equal sub-areas of $0.005° \times 0.005°$, lying within a 95% confidence interval of 500 bootstrap solutions. Fig. A2 presents the gridding of the area and the distribution of the focal mechanisms.

Appendix B.

B.1. Spatiotemporal evolution of the swarm

The spatiotemporal model in Fig. B1 presents the projection of epicenters on a line that passes through the middle of the spatial sequence at N110° E azimuth (aa′ profile shown in Fig. 8B) with respect to the time from origin time (May 21st, *X*-axis). The vertical axis represents the relative distance of each event from a reference point (Y_o) on the projection line. Two reference points, Y_oA and Y_oB were considered, each representing the location of the first

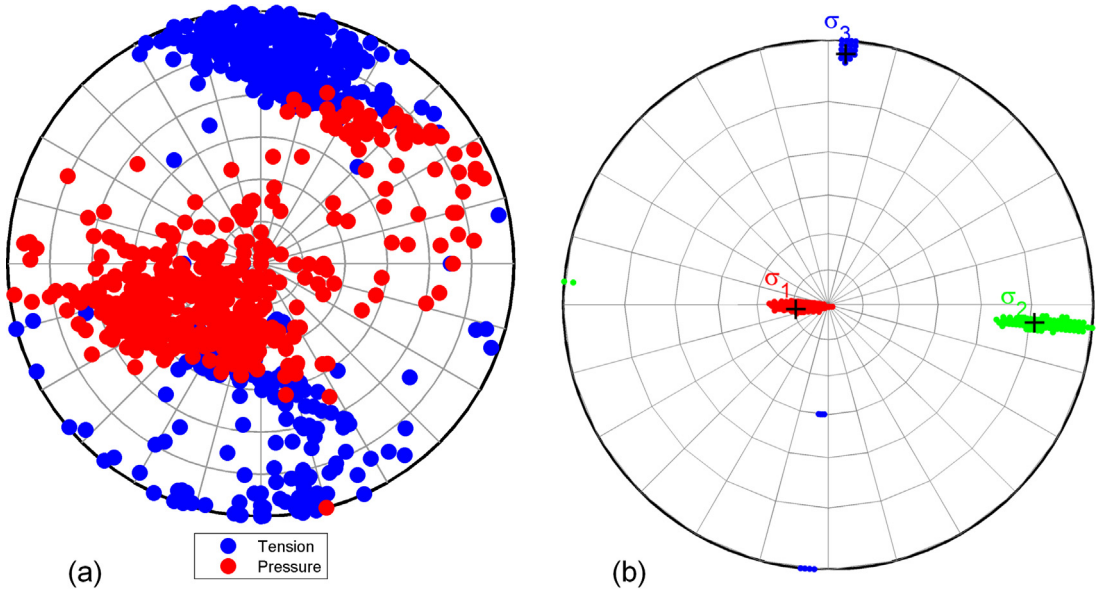

Fig. A1. (a) Stereonet showing the orientation and plunge of P- (pressure) and T- (tension) axes for 826 reliable focal mechanisms. (b) Average stress field pattern derived from the inversion of 826 focal mechanisms regarding the seismicity clusters in 1991 and 2013. The uncertainties were determined assuming 95% confidence intervals.

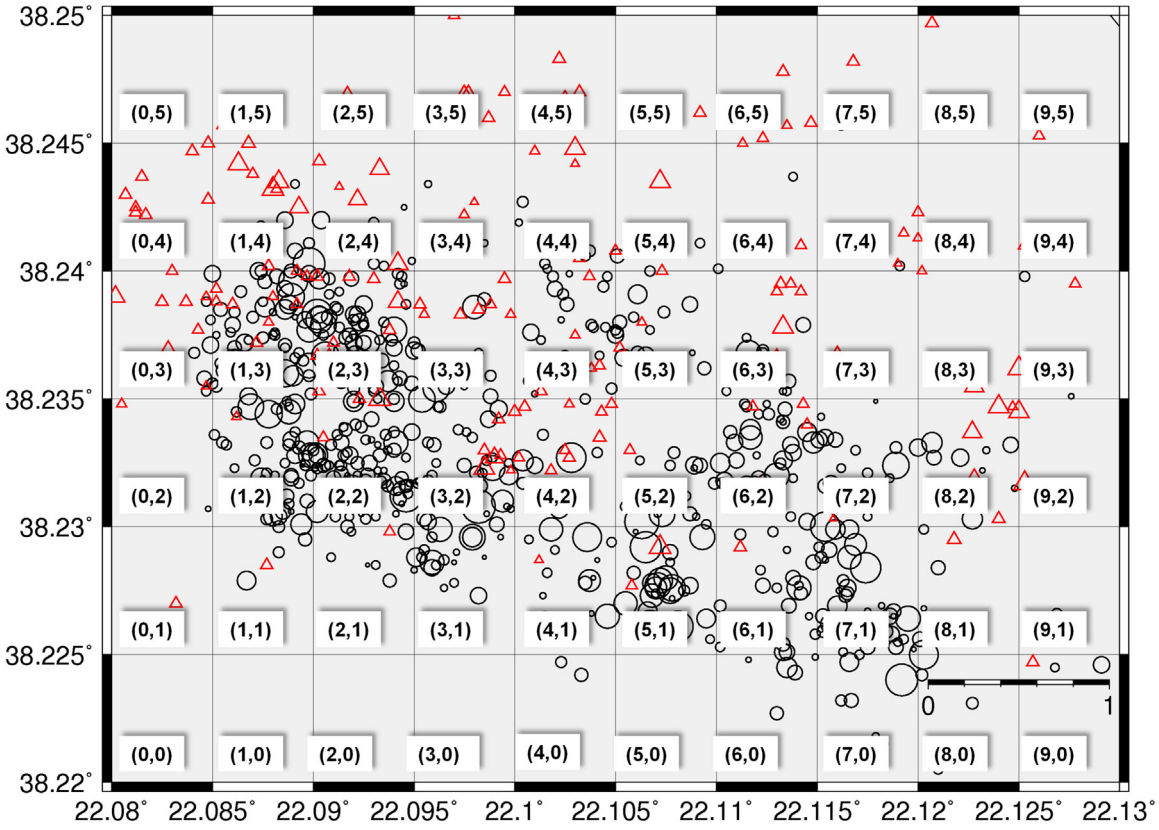

Fig. A2. Gridding setup for the 2D stress field inversion. Symbols denote epicenters of 826 reliable focal mechanisms. [Open red triangles]: focal mechanisms from the 1991 experiment (Rigo et al., 1996; Papadimitriou et al., 1994); [Open black circles]: focal mechanisms computed for the 2013 seismic activity.

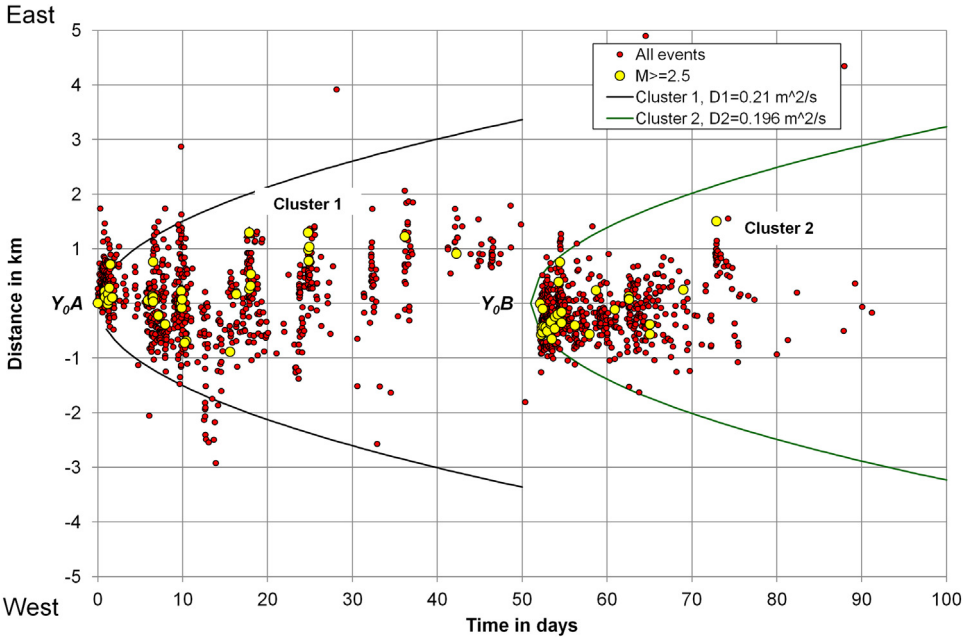

Fig. B1. Spatiotemporal diagram of the Aigion 2013 activity. The vertical axis represents the distance of the events on the projection line aa′ shown in Fig. 8B, with respect to two reference points representing the projection of the first significant event for each phase. Positive and negative Y values represent positions toward the east and the west with respect to the reference events. The horizontal axis denotes the relative time from the origin time. The starting points for the two phases were considered for a $M_L = 2.5$ event that occurred on 21/5/2013 ($X = 0$, Y_0A) and for a $M_L = 2.6$ event that occurred on 13/7/2013 ($X = 52$, Y_0B), respectively. The axis to the right indicates the relative position of phase B with respect to phase A. The envelope parabolic curves correspond to the possible position of the seismicity front with respect to a source at the same position as the 21/5 and 13/7 events, defined for a hydraulic diffusivity of 0.21 and 0.196 $m^2\ s^{-1}$, respectively.

significant event of each phase. Y_oA corresponds to a $M_L = 2.5$ event that occurred on May 21st, assumed as the origin time of the swarm (t_o) and Y_oB corresponds to a $M_L = 2.6$ event that occurred on July 13th, at the start of phase B. Regarding the first part of the swarm (phase A), during the first 10 days, the seismicity front slightly propagated for almost 0.5 km to the west, while the eastern segment remained active for a distance of about 1.8 km. On day 13, the seismicity front propagated another ~1.5 km to the west and reached at distance 3 km west of the starting point (Y_oA). At the same time, the eastern patch was inactive. On day ~15 the western patch became inactive and the rupture gradually migrated to the east until day 50, when seismicity was entirely confined at the eastern segment. It is worth mentioning that the migration diminished after day 25 (~June 17th). Between days 50–52 in the X-axis a period of total quiescence is observed and on day 52 (July 13th) phase B starts with the apparent seismicity shifting toward the western part (Y_oB). The outbreak of phase B, strongly clustered both in time and space, lasted ~17 days and it is confined on the western part, having a total length of 2 km. Interestingly, the pattern between days 0–15 is repeated between days 16–75, magnified by ~400% in time, but not in space.

We investigated the evolution of the 2013 activity following the approach of Shapiro et al. (1997) in order to accommodate the depiction of a possible fluid driven mechanism. The envelopes in Fig. B1 correspond to the distance of the seismicity front $r = r(t)$ (Eq. (1)) relative to the phase initiation times ($t - t_o$)

$$r(t) = \sqrt{4\pi D(t - t_o)} + y_o \quad (1)$$

corresponding to May 21st for phase A and July 13th for phase B, assuming a hydraulic diffusivity of 0.21 $m^2 s^{-1}$ and 0.196 $m^2 s^{-1}$, respectively. These hydraulic diffusivity values are compatible with the ones found by Pacchiani and Lyon-Caen (2010) for the 2001 swarm which took place a few km south of Aigion.

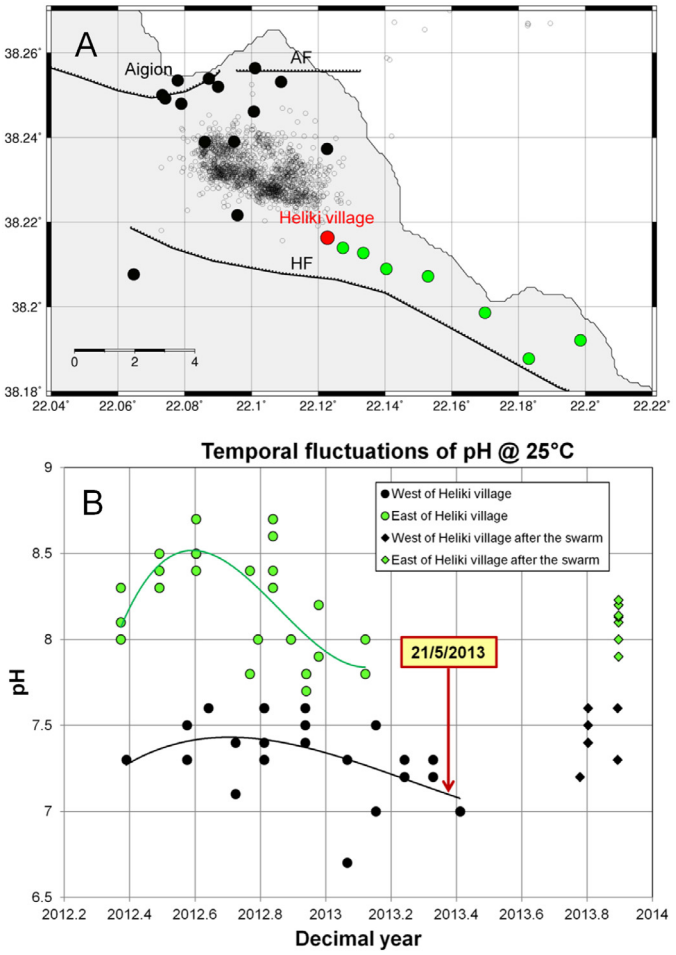

Fig. B2. (A) Locations of water samplings (solid circles). Empty black circles denote the relocated epicenters of the 2013 swarm. (B) Temporal fluctuation of the pH for the two types of table water. Solid black and green circles denote measurements west and east of Heliki village, respectively. The red arrow denotes the initiation of the swarm on May 21st 2013.

B.2. Geochemical data analysis

The available geochemical data for this study were provided by the Aigion Municipal Authority and contain the results on the pH values of water analyses from various aquifers and artesian wells located at several positions in and around the activated area. Unfortunately, the water sampling frequency, which was once per month before the initiation of the 2013 seismic activity, was reduced to once every three months after June 2013.

Fig. B2 summarizes the results and clearly illustrates two types of water sources based on the measured pH values. Samples taken west of Heliki exhibit significantly and systematically lower pH values with respect to water samples taken east of Heliki (Fig. B2A). This is most likely due to the two different water sources, the Selinous and Kerinitis rivers which supply the aquifers of the western and eastern areas, respectively. The most important observation is an overall decrease of pH for both water sources prior to the initiation of the seismic activity. This reduction of the pH values initiated at ~2012.72 and continued with almost a linear trend until ~2013.4, which is the time of the initiation of the swarm on May 21st. Data becomes available again at 2013.8 (end of October 2013) which shows pH values similar to those measured prior to the initiation of the 2013 swarm.

References

Armijo, R., Meyer, B., King, G.C.P., Rigo, A., Papanastassiou, D., 1996. Quaternary evolution of the Corinth Rift and its implications for the Late Cenozoic evolution of the Aegean. Geophys. J. Int. 126, 11–53.

Avallone, A., Briole, P., Agatza, Balodimou, A.M., et al., 2004. Analysis of eleven years of deformation measured by GPS in the Corinth Rift Laboratory area. C.R. Geosci. 336, 301–311.

Beckers, A., Hubert-Ferrari, A., Beck, C., Bodeux, S., Tripsanas, E., Sakellariou, D., De Batist, M., 2015. Active faulting at the western tip of the Gulf of Corinth, Greece, from high-resolution seismic data. Mar. Geol. 360, 55–69.

Bell, R., McNeill, L.C., Bull, J.M., Henstock, T.J., 2008. Evolution of the western Gulf of Corinth continental rift, Greece. Geol. Soc. Am. Bull. 120, 156–178.

Bell, R.E., McNeill, L.C., Bull, J.M., Henstock, T.J., Collier, R.E.L., Leeder, M.R., 2009. Fault architecture, basin structure and evolution of the Gulf of Corinth Rift, Central Greece. Basin Res. 21, 824–855.

Bell, R.B., McNeill, L.C., Henstock, T.J., Bull, J.M., 2011. Comparing extension on multiple and depth scales in the Corinth Rift, Central Greece. Geophys. J. Int. 186, 463–470.

Bernard, P., Lyon-Caen, H., Briole, P., Deschamps, A., Boudin, F., Makropoulos, K., Papadimitriou, P., Lemeille, F., Patau, G., Billiris, H., Paradissis, D., Papazissi, K., Castarede, H., Charade, O., Nercessian, A., Avallone, A., Pacchiani, F., Zahradnik, J., Sacks, S., Linde, A., 2006. Seismicity, deformation and seismic hazard in the western rift of Corinth: new insights from the Corinth Rift Laboratory (CRL). Tectonophysics 426, 7–30.

Bernard, P., Briole, P., Meyer, B., Lyon-Caen, H., Gomez, J.-M., Tiberi, C., Berge, C., Cattin, R., Hatzfeld, D., Lachet, C., Lebrun, B., Deschamps, A., Courboulex, F., Larroque, C., Rigo, A., Massonnet, D., Papadimitriou, P., Kassaras, J., Diagourtas, D., Makropoulos, K., Veis, G., Papazisi, E., Mitsakaki, C., Karakostas, V., Papadimitriou, E., Papanastassiou, D., Chouliaras, M., Stavrakakis, G., 1997. The Ms = 6.2, June 15, 1995 Aigion earthquake (Greece): evidence for low angle normal faulting in the Corinth rift. J. Seismol. 1, 131–150.

Bourouis, S., Cornet, F.H., 2009. Microseismic activity and fluid fault interactions: some results from the Corinth Rift Laboratory (CRL), Greece. Geophys. J. Int. 178 (1), 561–580.

Briole, P., Rigo, A., Lyon-Caen, H., Ruegg, J.C., Papazissi, K., Mitsakaki, C., Balodimou, A., Veis, G., Hatzfeld, D., Deschamps, A., 2000. Active deformation of the

Corinth rift, Greece: Results from repeated Global Positioning System surveys between 1990 and 1995. J. Geoph. Res. 105 (B11), 25.605–25.625, http://dx.doi.org/10.1029/2000JB900148
Chousianitis, K., Ganas, A., Evangelidis, C.P., 2015. Strain and rotation rate patterns of mainland Greece from continuous GPS data and comparison between seismic and geodetic moment release. J. Geophys. Res. Solid Earth 120, 3909–3931, http://dx.doi.org/10.1002/2014JB011762
Clarke, P.J., Davies, R.R., England, P.C., Parson, B., Billiris, H., Paradissis, D., Veis, G., Cross, P.A., Denys, P.H., Ashkenazi, V., Bingley, R., Kahle, H.-G., Muller, M.-V., Briole, P., 1998. Crustal strain in central Greece from repeated GPS measurements in the interval 1989-1997. Geophys. J. Int. 135, 195–214, http://dx.doi.org/10.1046/j.1365-246X.1998.00633.x
Collier, R., Jones, G., 2003. Rift sequences of the Southern margin of the Gulf of Corinth (Greece) as exploration/production analogues. In: AAPG International Conference Barcelona, Search and Discovery Article#90017.
Corti, G., 2009. Continental rift evolution: from rift initiation to incipient break-up inthe Main Ethiopian Rift, East Africa. Earth Sci. Rev. 96, 1–53.
Corti, G., 2012. Evolution and characteristics of continental rifting: analog modeling-inspired view and comparison with examples from the East African Rift System. Tectonophysics 522–523, 1–33.
De Martini, P.M., Pantosti, D., Palyvos, N., Lemeille, F., McNeill, L., Collier, R., 2004. Slip rates of the Aigion and Eliki faults from uplifted marine terraces, Corinth Gulf, Greece. C.R. – Geosci. 336, 325–334.
Doan, M.L., Cornet, F.H., 2007. Thermal anomaly near the Aigio fault, Gulf of Corinth, Greece, maybe due to convection below the fault. Geophys. Res. Lett. 34, L06314, http://dx.doi.org/10.1029/2006GL028931
Doutsos, T., Kontopoulos, N., Poulimenos, G., 1988. The Corinth-Patras rift as the initial stage of continental fragmentation behind an active island arc (Greece). Basin Res. 1, 177–190.
Ford, M., Rohais, S., Williams, E.A., Bourlange, S., Jousselin, D., Backert, N., Malartre, F., 2013. Tectono-sedimentary evolution of the western Corinth rift (Central Greece). Basin Res. 25, 3–25, http://dx.doi.org/10.1111/j.1365-2117.2012.00550.x
Goebel, T.H.W., Schorlemmer, D., Becker, T.W., Dresen, G., Sammis, C.G., 2013. Acoustic emissions document stress changes over many seismic cycles in stick-slip experiments. Geophys. Res. Lett. 40 (10), 2049–2054, http://dx.doi.org/10.1002/grl.50507
Gutenberg, R., Richter, C.F., 1944. Frequency of earthquakes in California. Bull. Seismol. Soc. Am. 34, 158–188.
Hainzl, S., Ogata, Y., 2005. Detecting fluid signals in seismicity data through statistical earthquake modelling. J. Geophys. Res. 110, B05S07, http://dx.doi.org/10.1029/2004JB003247
Hardebeck, J.L., Michael, A.J., 2006. Damped regional-scale stress inversions: methodology and examples for southern California and the Coalinga aftershock sequence. J. Geophys. Res. Solid Earth 111 (B11), B11310, http://dx.doi.org/10.1029/2005JB004144
Hatzfeld, D., Karakostas, V., Ziazia, M., Kassaras, I., Papadimitriou, E., Makropoulos, K.C., Voulgaris, N., Papaioannou, C., 2000. Microseismicity and faulting geometry in the Gulf of Corinth (Greece). Geophys. J. Int. 141, 438–456.
Ibs-von Seht, M., Plenefisch, T., Klinge, K., 2008. Earthquake swarms in continental rifts – a comparison of selected cases in America, Africa and Europe. Tectonophysics 452, 66–77.
Ishimoto, M., Iida, K., 1939. Observations of earthquakes registered with the microseismograph constructed recently. Bull. Earthq. Res. Inst. 17, 443–478.
Jolivet, L., 2001. A comparison of geodetic and finite strain pattern in the Aegean, geodynamic implications. Earth Planet. Sci. Lett. 187, 95–104.
Kagan, Y., 1999. Universality of the seismic moment-frequency relation. Pure Appl. Geophys. 155, 537–574.
Kapetanidis, V., Papadimitriou, P., Makropoulos, K., May 2010. A cross-correlation technique for relocation of seismicity in the western Corinth rift. In: Bull. Geol. Soc. Greece, Proc. of the 12th International Congress, XLIII, No. 4, Patras, pp. 2015–2025.
Kissling, E., 1995. Velest User's Guide, Internal Report. Institute of Geophysics, ETH, Zurich.
Kissling, E., Ellsworth, W.L., Eberhart-Phillips, D., Kradolfer, U., 1994. Initial reference models in local earthquake tomography. J. Geophys. Res. 99, 19635–19646.
Klein, R.W., 2000. Hypocenter location program HYPOINVERSE, I, Users guide to versions 1, 2, 3, and 4. U.S. Geol. Surv. Open File Rep., pp. 78–694.
Lambotte, S., Lyon-Caen, H., Bernard, P., Deschamps, A., Patau, G., Nercessian, A., Pacchiani, F., Bourouis, F., Drilleau, M., Adamova, P., 2014. Reassessment of the rifting process in the Western Corinth Rift from relocated seismicity. Geophys. J. Int. 197, 1822–1844, http://dx.doi.org/10.1093/gji/ggu096
Lyon-Caen, H., Papadimitriou, P., Deschamps, A., Bernard, P., Makropoulos, K., Pacchiani, F., Patau, G., 2004. First results of the CRLN seismic network in the western Corinth Rift: evidence for old fault reactivation. C.R. Geosci. 336 (4–5), 343–353.
Makropoulos, K., Kaviris, G., Kouskouna, V., 2012. An updated and extended earthquake catalog for Greece and adjacent areas since 1900. Nat. Hazards Earth Syst. Sci. 12, 1425–1430, http://dx.doi.org/10.5194/nhess-12-1425-2012
Martínez-Garzón, P., Kwiatek, G., Ickrath, M., Bohnhoff, M., 2014. MSATSI: A MATLAB package for stress inversion combining solid classic methodology, a new simplified user-handling and a visualization tool. Seismol. Res. Lett. 85, 4, http://dx.doi.org/10.1785/0220130189
McNeill, L., Cotterill, C., Stefatos, A., Henstock, T., Bull, J., Collier, R., Papatheoderou, G., Ferentinos, G., Hicks, S., 2005a. Active faulting within the offshore western Gulf of Corinth, Greece: implications for models of continental rift deformation. Geology 33, 241–244.
McNeill, L.C., Collier, R.E., De Martini, Ll., Pantosti, P.M., D'Addezio, D.G., 2005b. Recent history of the Eastern Eliki Fault, Gulf of Corinth: geomorphology, palaeoseismology and impact on palaeoenvironments. Geophys. J. Int. 161 (1), 154–166.
McNeill, L.C., Cotterill, C.J., Bull, J.M., Henstock, T.J., Bell, R., Stefatos, A., 2007. Geometry and slip rate of the Aigion fault, a young normal fault system in the western Gulf of Corinth. Geology 35, 355–358, http://dx.doi.org/10.1130/G23281A.1
Micarelli, L., Moretti, I., Daniel, J.M., 2003. Structural properties of rift related normal faults: the case of the Gulf of Corinth, Greece. J. Geodyn. 36, 275–303.
Mignan, A., Chouliaras, G., 2014. 50 years of seismic network performance in Greece (1964–2013): spatiotemporal evolution of the completeness magnitude. Seismol. Res. Lett. 85, 657–667, http://dx.doi.org/10.1785/0220130209
Mogi, K., 1963. Some discussions on aftershocks, foreshocks, and earthquake swarms: the fracture of a semi-infinite body caused by an inner stress origin and its relation to the earthquake phenomenon. Bull. Earthq. Res. Inst. Univ. Tokyo 41, 615–658.
Moretti, I., Sakellariou, D., Lykousis, V., Micarelli, L., 2003. The Gulf of Corinth: an active half graben? J. Geodyn. 36, 323–340.
Nanjo, K.Z., Hirata, N., Obara, K., Kasahara, K., 2012. Decade-scale decrease in b value prior to the M9-class 2011 Tohoku and 2004 Sumatra quakes. Geophys. Res. Lett. 39, http://dx.doi.org/10.1029/2012GL052997
Neumann, G.A., Zuber, M.T., 1995. A continuum approach to the development of normal faults. In: Daemen, J.J.K., Schultz, R.A. (Eds.), Rock Mechanics. Balkema, Rotterdam, pp. 191–198, ISBN-905410526.
Nyst, M., Thatcher, W., 2004. New constraints on the active tectonic deformation of the Aegean. J. Geophys. Res. 109, B11406.
Ogata, Y., Zhuang, J., 2006. Space-time ETAS models and an improved extension. Tectonophysics 413, 13–23, http://dx.doi.org/10.1016/j.tecto.2005.10.016
Ogata, Y., 1988. Statistical models for earthquake occurrences and residual analysis for point processes. J. Am. Stat. Assoc. 83, 9–27.
Ogata, Y., 1992. Detection of precursory seismic quiescence before major earthquakes through a statistical model. J. Geophys. Res. 97, 19845–19871.
Pacchiani, F., Lyon-Caen, H., 2010. Relocation and spatio-temporal evolution of the 2001 Agios Ioannis earthquake swarm (Corinth rift, Greece). Geophys. J. Int. 180, 59–72.
Palyvos, N., Lemeille, F., Sorel, D., Pantosti, D., Pavlopoulos, K., 2008. Geomorphic and biological indicators of paleoseismicity and Holocene uplift rate at a coastal normal fault footwall (western Corinth Gulf, Greece). Geomorphology 96, 16–38.
Papadimitriou, P., Kassaras, A., Rigo, A., Lyon-Caen, H., Hatzfeld, D., Makropoulos, K.C., Drakopoulos, J., 1994. Source parameters of large and small earthquakes in Corinth Gulf (C. Greece). In: Proc. ESC XXIV Gen. Assembly, Athens, pp. 848–858.
Papadimitriou, P., Voulgaris, N., Kassaras, I., Kaviris, G., Delibasis, N., Makropoulos, K., 2002. The Mw = 6.0, September 7, 1999 Athens earthquake. Natl. Hazards 27, 15–33.
Papazachos, B.C., Papazachou, C.B., 2003. In: Ziti, P. (Ed.), The Earthquakes of Greece. Thessaloniki, Greece (in Greek).
Rigo, A., Lyon-Caen, H., Armijo, R., Deschamps, A., Hatzfeld, D., Makropoulos, K., Papadimitriou, P., Kassaras, I., 1996. A microseismic study in the western part of the Gulf of Corinth (Greece): implications for large-scale normal faulting mechanisms. Geophys. J. Int. 126, 663–688.
Schmidt, J., 1879. Studien uber Erdbeben. Carl Schottze, Leipzig, pp. 68–83.
Schorlemmer, D., Wiemer, S., Wyss, M., 2005. Variation of earthquake-size distribution across different stress regimes. Nature 437, 539–542.
Shapiro, S.A., Huenges, E., Borm, G., 1997. Estimating the crust permeability from fluid-injection-induced seismic emission at the KTB site. Geophys. J. Int. 131, F15–F18.
Sorel, D., 2000. A Pleistocene and still-active detachment fault and the origin of the Corinth-Patras rift, Greece. Geology 28 (1), 83–86, 10.1130/0091-7613(2000)28<83:APASDF>2.0.CO;2.
Taylor, B., Weiss, J.R., Goodliffe, A.M., Sachpazi, M., Laigle, M., Hirn, A., 2011. The structures, stratigraphy and evolution of the Gulf of Corinth rift, Greece. Geophys. J. Int., http://dx.doi.org/10.1111/j.1365-246X.2011.05014.x
Utsu, T., Ogata, Y., Matsu, R.S., 1995. The centenary of the Omori formula for a decay law of aftershock activity. J. Phys. Earth 43, 1–33.
Utsu, T., Ogata, Y., 1997. Statistical Analysis of Seismicity (SASeis) for Seismicity. IASPEI Software Library 6, 13–94.
Van Wijk, J.W., 2005. Role of weak zone orientation in continental lithosphere extension. Geophys. Res. Lett. 32, http://dx.doi.org/10.1029/2004GL022192
Vannucci, G., Gasperini, P., 2004. The new release of the database of Earthquake Mechanisms of the Mediterranean Area (EMMA version 2). Ann. Geophys. 47, 303–327.
Waldhauser, F., Ellsworth, W.L., 2000. A double-difference earthquake location algorithm: method and application to the Northern Hayward Fault. Bull. Seism. Soc. Am. 90 (6), 1353–1368.
Waldhauser, F., Ellsworth, W.L., 2002. Fault structure and mechanics of the Hayward Fault, California, from double-difference earthquake locations. J. Geophys. Res. 107 (B3), http://dx.doi.org/10.1029/2000JB000084

Wiemer, S., Wyss, M., 2000. Minimum magnitude of complete reporting in earthquake catalogs: examples from Alaska, the Western United States, and Japan. Bull. Seism. Soc. Am. 90, 859–869.
Wiemer, S., 2001. A software package to analyze seismicity: ZMAP. Seism. Res. Lett. 72, 373–382.
Ziegler, P.A., Cloetingh, S.A.P.L., 2004. Dynamic processes controlling evolution of rifted basins. Earth-Sci. Rev. 64, 1–50.
Zoback, M.D., Harjes, H.-P., 1997. Injection-induced earthquakes and crustal stress at 9 km depth at the KTB deep drilling site, Germany. J. Geophys. Res. Atmos. 102, 18477–18491, B8.
Zoback, M.D., 1992. First and second order patterns of stress in the lithosphere: the World Stress Map project. J. Geophys. Res. 97, http://dx.doi.org/10.1029/92JB00132.